Chem. Senses 32: 215–223, 2007

doi:10.1093/chemse/bjl047
Advance Access publication January 13, 2007

Modeling Inspiratory and Expiratory Steady-State Velocity Fields in the Sprague-Dawley Rat Nasal Cavity

Geoffrey C. Yang[1,2], Peter W. Scherer[1] and Maxwell M. Mozell[3]

[1]Department of Bioengineering, School of Engineering and Applied Science, University of Pennsylvania, Philadelphia, PA 19104, USA and [3]Department of Neuroscience and Physiology, State University of New York, Upstate Medical University, Syracuse, NY 13210, USA
[2]Present address: Affymetrix, Inc., 3420 Central Expressway, Santa Clara, CA 95051, USA

Correspondence to be sent to: Peter W. Scherer, Department of Bioengineering, School of Engineering and Applied Science, University of Pennsylvania, 240 Skirkanich Hall/6321, 210 S 33rd Street, Philadelphia, PA 19104, USA. e-mail: scherer@seas.upenn.edu

Abstract

Distribution patterns of odorant molecules in the rat nasal olfactory region depend in large part on the detailed airflow patterns in the nasal cavity, which in turn depend on the anatomical structure. To investigate these flow patterns, we constructed an anatomically accurate finite element model of the right nasal cavity of the Sprague-Dawley rat based on horizontal (anterior–posterior) nasal cast cross sections. By numerically solving the fluid mechanical momentum and continuity equations using the finite element method, we studied the flow distribution and the complete velocity field for both inspiration and expiration throughout the nasal cavity under physiological flow rates of resting breathing and sniffing. Detailed velocity profiles, volumetric flow distributions, and streamline patterns for quasi-steady airflow are presented. S-shaped streamlines passing through the olfactory region are found to be less prevalent during expiratory than inspiratory flow leading to trapping and an increase in odorant molecule retention in the olfactory region during sniffing. The rat nasal velocity calculations will be used to study the distribution of odorant uptake onto the rat olfactory mucosa and compare it with the known anatomic location of some types of rat olfactory receptors.

Key words: finite element analysis, nasal airflow, olfactory mucosa, sniffing, streamline

Introduction

The rat nasal cavity provides a passage for ambient air as it flows into the lower respiratory tract. Transport of odorant molecules and bulk airflow in the nasal cavity are interrelated physical phenomena, which depend upon the anatomical structure of the airway.

The main physiological functions of the nose are: 1) humidification and warming of inhaled air to near full water saturation and body core temperature, 2) protection of the lower airway from inhaled material, and 3) transduction of the odorant absorption into action potentials generated in olfactory neurons leading to the brain. Nasal anatomy and the resultant patterns of nasal airflow determine the performance of these physiological functions. Study of these flow patterns is useful in characterizing all nasal transport processes and aids in particular in understanding olfaction.

The rat nasal airway is divided sagittally by the nasal septum into 2 cavities (fossae) (Uraih and Maronpot 1990). Air enters through 2 exterior openings—the external nares, which wrap around and open to the side of the snout forming the anterior twists or spirals. The nasal vestibule is defined as roughly the anterior 6 mm in from the external naris openings. The bony nasal septum terminates about 30–35 mm back from the external nares. At this point, both sides of the nasal cavity merge through a landmark called the septal window, which marks the beginning of the nasopharyngeal meatus (passageway) (Kelemen 1947).

The olfactory region of the rat nasal cavity is located dorsoposteriorly and is composed of a large number of branch-like scrolled turbinate structures that project from the posterior and lateral walls of the rat nose (Figures 1 and 6). The nasopharyngeal airway can be divided anterioposteriorly into 5 regions: the nares, maxilloturbinates, ethmoturbinates, pharynx, and larynx (Schreider 1983). Mery et al. (1994) proposed a system of classification of the 6 ethmoturbinates for rats and mice, in which they were numbered sequentially from the most dorsal turbinate and moving ventrally

along the lateral wall of the nasal cavity. The dorsal meatus extends into the dorsal part of the ethmoid recess, whereas the middle meatus terminates at the maxillary sinus. Finally, the ventral meatus extends along the floor of the nasal cavity and terminates at the nasopharyngeal meatus (Uraih and Maronpot 1990).

The use of the computed velocity field found through the highly detailed modeling technique of computational fluid dynamics (CFD) to simulate odorant uptake in the olfactory region was motivated by the need for anatomical accuracy and the link to the general anatomy of olfactory receptor (OR) gene expression zones, enabling us to test the hypotheses of olfactory mechanisms involving these zones. In this paper, we focus on olfactory flow and emphasize both inspiratory and expiratory flow distribution in the olfactory region of the rat nasal cavity.

The construction of 3-dimensional (3D) finite element models of the rat nasal cavity has been aided by information developed from neuroanatomical research and inhalation toxicology studies. Several in vitro approaches have also been used to obtain airflow patterns in the nasal cavity. The small dimensions of the real rat nasal cavity, however, limit the accuracy and application of experimental velocity measurement techniques. Morgan and colleagues (Patra et al. 1986; Morgan et al. 1991) investigated airflow patterns in steady flow through rat nasal cavity models. They performed a series of experiments and flow simulations on the F344 rat nasal cavity using water-dye streams flowing steadily in hollow acrylic nasal casts (Morgan et al. 1991). Water flow rates were determined by matching the Reynolds number (N_{Re}) in the cast with that of the physiological airflow in the real rat nasal cavity. Due to size limitation, video analysis of dye streaklines was performed instead of detailed velocity measurements to determine the location of major flow streams. Later, the regional flow velocity in these streams was measured using frame-by-frame video analysis (Kimbell et al. 1990, 1993). The location of major airflow streams and points of impaction onto the airway walls in the anterior respiratory tract were shown to correlate with the sites of lesions after inhalation exposure to formaldehyde gas.

Kimbell et al. (1993) also developed a 3D finite element model of the right nasal cavity of the F344 rat based on serial coronal sections using the CFD software package FIDAP. They later extended the model to include the more complicated, posterior convoluted turbinates and simulated steady inspiratory airflow in all regions throughout the nasal cavity (Kimbell et al. 1997). Their FIDAP mesh was composed of 84 coronal cross sections, which were selected on the basis of critical anatomical features from a total set of 596 physical sections cut at 50-μm intervals. Uniform (plug flow) velocity profiles were applied at the external nares of the rat model at different flow rates between 100–905 ml/min (N_{Re} = 42–380). Kimbell et al. (1993) numerically reproduced the experimentally observed flow stream locations for different physiological flow rates for resting inspiratory breathing and validated their FIDAP model using dye streaklines in hollow nasal molds. Volumetric flow rates on 2 coronal sections, one anterior to and the other in the ethmoid recesses, were apportioned to determine the percentage of total volumetric flow (anterior) or percentage of total positive ethmoid flow (ethmoid) in each of the subregions.

From a quantitative analysis of sniffing strategy during odor detection tasks, Youngentob et al. (1987) determined the structures of sniffing bouts in rats. A sniffing bout begins with 1 or 2 inspirations before an expiration and then is followed by alternating inspiration and expiration. In this paper (see also Yang 1999; Zhao et al. 2006), we have numerically modeled inspiration and expiration in the rat nasal cavity under physiological flow rates of resting breathing and at higher sniffing velocities. Detailed velocity profiles, volumetric flow distributions, and streamline patterns for quasi-steady airflow throughout the nasal cavity are presented with an emphasis on the olfactory region.

Materials and Methods

A large male Sprague-Dawley rat was used to prepare for the polyurethane cast of the nasal cavity in this study. The cast was prepared at Dr G. Neufeld's laboratory at the Philadelphia VA Medical Center (Philadelphia, PA) and was sectioned horizontally by a milling machine.

Model geometry and mesh generation

A 3D anatomically accurate mesh of the right rat nasal cavity (Figure 1A) was developed using the CFD software package

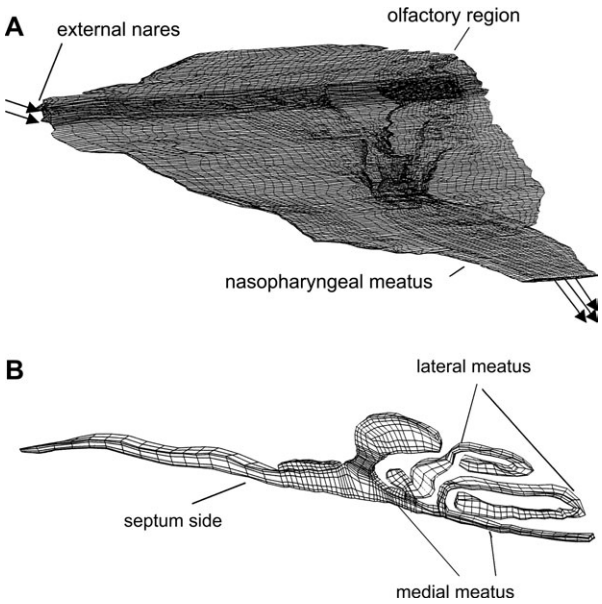

Figure 1 Reconstruction of the right side of the nasal cavity of the Sprague-Dawley rat. **(A)** Septal external view of the 3D mesh. Arrows show the direction of the inspiratory airflow. **(B)** Finite element mesh of a horizontal slice spanning the planes 47 and 48 is shown.

FIDAP (Fluid Dynamics Analysis Package, Fluent, Inc., Lebanon, NH), which uses the finite element method (FEM). The mesh was based on a set of photomicrographs of horizontal (anterior–posterior) sections (each 125 μm thick) of a polyurethane cast of a Sprague-Dawley rat nasal cavity.

The nasal passage outlines of 88 horizontal sections were traced using a digitizing tablet (SummaSketch II Plus, Summagraphics Corp., Fairfield, CT). Coordinates of "key points" defining the curved edge of each cross section were processed and imported into the mesh-generating preprocessor module FIMESH. Serial-sections were then aligned one next to the other in 3D space (Figure 1B).

Following the meshing scheme, the physical region was divided into 6-sided, 8-node brick elements. The resultant computational domain contains 134 014 nodes and 107 024 brick elements. The total number of finite elements and nodes used in the model was optimized to achieve accurate results and save computation time. Cross-section alignment was adjusted by reviewing the exterior outline contour of the structure and by comparing the individual FIDAP-generated coronal cross sections. Common artifacts, such as bubbles in the cast, were detected and corrected by comparison with the photomicrographs. The model then underwent an iterative development process until a smooth outline was reached and in general no flaws could be detected by visual inspection. The mesh was also compared with coronal sections at various locations in the F344 rat nasal cavity drawn by Mery et al. (1994) and found to be similar.

"In silico" coronal planes selected from the right nasal cavity structure (Table 1) are used in comparing our simulated results with the analysis results from the literature, particularly with the work of Kimbell et al. (1997). A comparison of Kimbell's K6 and K23 sections and our corresponding in silico sections shows good agreement in shape. Details of some of the ethmoid turbinates, that is, planes 190 and 214 appeared not totally complete after reconstruction. This inaccuracy was most likely due to some minor artifacts in part of these anterior–posterior photomicrographs and subsequent errors during alignment of the photomicrographs and digitization of the nasal passage outlines. However, the resultant impact of those induced "blind" ducts in the olfactory region on the total airflow is likely to be negligible in this study.

Table 1 Comparison of the numbering system of the coronal sections

Coronal section ID		
Yang (1999)	Kimbell et al. (1997)	Distance (cm)[a]
126	K6	1.58
149		1.86
163		2.04
176		2.2
188		2.35
200	K23	2.5
226		2.83
241		3.01

[a]Distance is calculated from the anterior tip of nose to each section.

Governing equations and boundary conditions

The governing equations for incompressible steady airflow are the Navier-Stokes equations,

$$\rho(\underline{\boldsymbol{u}} \cdot \nabla \underline{\boldsymbol{u}}) = -\nabla p + \mu \nabla^2 \underline{\boldsymbol{u}}, \quad (1)$$

and the continuity equation,

$$\nabla \cdot \underline{\boldsymbol{u}} = 0, \quad (2)$$

where $\underline{\boldsymbol{u}}$, μ, ρ are the velocity vector, dynamic viscosity, and density of air, respectively; p is the pressure; and ∇and ∇^2 are the gradient and Laplace operators, respectively. Both equations were solved numerically and simultaneously to determine airflow velocities and pressures. The walls of the nasal cavity were assumed rigid, and the air velocity was assumed to be zero at the interface between air and the surface of the mucus lining the nasal cavity. Uniform (plug flow) velocity profiles were applied at the external naris (inlet) of the rat model for the simulation of inspiratory flow at different flow rates. The application of a parabolic velocity profile with equivalent flow rates yielded no significant difference in the computed downstream velocity profiles. At the outlet for inspiration—the end section of the nasopharyngeal meatus, a stress-free boundary condition (zero normal and tangential stresses) on the velocity field, which arises naturally from the application of the FEM, was applied. For the simulation of expiratory flow, a parabolic velocity profile was applied at the end section of the nasopharyngeal meatus (inlet) and a stress-free boundary condition was applied at the external naris (outlet).

The finite element mesh was used to calculate the velocity field for the following 3 half-nasal physiological flow rates—126, 252, and 504 ml/min, corresponding to uniform axial velocities (U) of 84, 168, and 336 cm/s, respectively (Youngentob et al. 1987). The corresponding values of the Reynolds number N_{Re} (N_{Re} = 94, 188, and 376, respectively) at the external naris cross section suggest that the assumption of laminar airflow in the rat nasal cavity is reasonable (Whitaker 1992). Unsteadiness in the flow can reasonably be neglected because the Strouhal number N_{St} is less than unity during both maximal sniffing and normal breathing at rest, and thus, a quasi-steady boundary layer in the airway can be established (Pedley et al. 1977). Details of how the Reynolds number and the Strouhal number are calculated are provided in the Appendix.

Solution methods

Within each mesh element, the independent variables were interpolated by shape or basis functions in terms of values

determined at the element nodal points. Continuity of dependent variables between adjacent elements was required when assembling the discretized equations for all elements in the entire domain. In order to save time and reduce computer file storage and CPU requirements, a segregated algorithm option (pressure projection version) was used to solve the large 3D nonlinear problem instead of using fully coupled methods, such as Newton-Raphson. The segregated solver creates a set of equations for a single degree of freedom at a time and cycles sequentially through all unknowns at each iterative step. The iterations were repeated until convergence was reached.

The convergence criterion used for the termination of velocity iterations was

$$\frac{\|\boldsymbol{u}_i - \boldsymbol{u}_{i-1}\|}{\|\boldsymbol{u}_i\|} \leq \text{tolerance}, \quad (3)$$

where $\boldsymbol{u}_i$ is the velocity solution vector at iteration i and $\|\cdot\|$is the root mean square norm summed over all the nodes of the mesh. For all norms of each dimension, the criteria have to be satisfied simultaneously to reach convergence. Bulk mass conservation of the flow was checked for the final solution to the nonlinear Navier-Stokes problem, yielding an error of less than 0.3% between inlet flow and outlet flow.

Results

As the main objective was to use the CFD technique in this numerical modeling work, all subsequent results demonstrate only simulated, not measured, velocity fields in the nasal cavity, unless otherwise specified.

Inspiratory flow

Streamlines

Streamlines help visualize the bulk flow patterns in the rat nose. At the flow rates for resting breathing and sniffing, streamlines for inspiratory flow were traced by introducing neutrally buoyant particles at the external naris and computing the particle trajectories as a result of the computed velocity field.

Five major inspiratory flow streams were predicted in the rat nasal cavity: dorsomedial (DM), dorsolateral (DL), middle (M), ventromedial (VM), and ventrolateral (VL) as were observed in the dye streakline studies of Morgan et al. (1991). The trajectories of our simulated streamlines were dependent upon the locations from which the particles were released on the external nares surface plane. For illustrative purpose, the boundary of the olfactory region, which is the most dorsal and posterior region in the nasal cavity, was diagrammatically marked on the sagittal section seen from the septal side. The boundary of the olfactory epithelium was based on a whole mount of the nasal septal epithelium that was stained with an antibody to olfactory marker protein by Ring and colleagues (Ring et al. 1997).

For release sites on the medial side of the external nares, simulated DM streamlines traced out S-shaped curves and entered the ethmoid recesses, whereas VM streamlines flowed along the floor of the nasal cavity. For release sites on the lateral side of the external naris, DL and VL streamlines passed through the DL meatus and VL meatus, respectively (Figures 2 and 3).

Our computed streamlines for inspiration were in general agreement with those found by Morgan et al. (1991) using video analysis and the simulated results from the FIDAP model of Kimbell et al. (1997). Simulated streams that originated from the lower ventral portion of the external naris generally passed along the nasal floor and exited through the nasopharyngeal meatus. Streams originating from the upper dorsal portion of the external naris generally took more circuitous S-shaped routes: streams entered the convoluted ethmoid recesses, then bent backward toward the external naris (reverse flow), and finally exited through the dorsal region of the nasopharyngeal meatus (Figure 3A).

Velocity profiles

Isovelocity color contours for the axial velocity component (u_x) in selected coronal sections for the inspiratory flow rate of 252 ml/min (Figure 4A) were compared with the results of Kimbell et al. (1997) for an inspiratory flow at 288 ml/min and showed general agreement. For example, on plane 200 (or K23), negative velocity (dark blue) was predicted

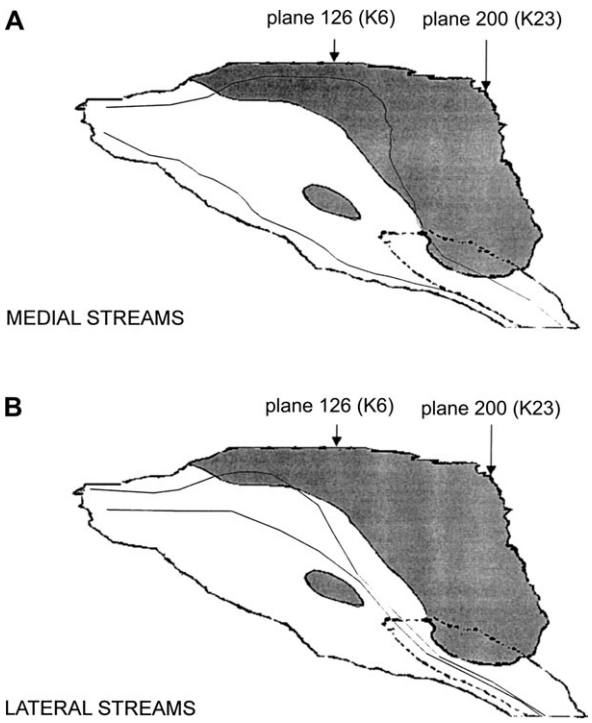

Figure 2 Numerically simulated trajectories of 4 major inspiratory flow streamlines at the physiological flow rate of 126 ml/min. Streamlines were traced by placing the release points near the **(A)** medial septal walls (medial streams DM and VM) and **(B)** lateral walls (lateral streams DL and VL) of the external naris plane. Dashed lines show the boundary of the septal window of the nasopharyngeal meatus.

in the ventral and lateral meati, which are surrounded by the ethmoturbinates IV, V, and VI, whereas the velocity in the dorsal meatus surrounded by the ethmoturbinates I, II, and III, was calculated as positive (red), as was shown by Kimbell and colleagues. In general, the velocities simulated by Kimbell and colleagues along the septum were somewhat higher than ours, but this is probably due to the fact that the septal airway slit was wider in the Kimbell model than in ours.

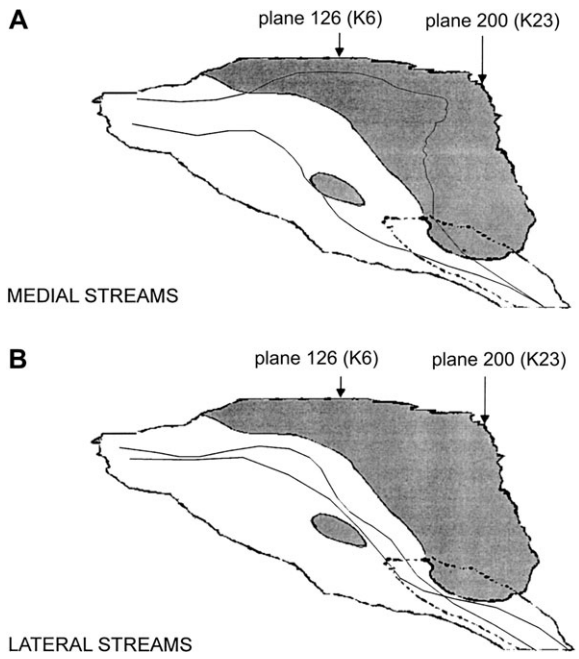

Figure 3 Simulated trajectories of the major inspiratory flow streamlines at 504 ml/min. The same release points on the external naris plane were used as in Figure 2.

We conclude that the main stream of the simulated bulk airflow (with the air speed ≅ 150 cm/s) passed ventrally through the passages and exited through the nasopharyngeal meatus without entering the ethmoid recesses (Table 2 and Figure 4A). The location of the major high-speed airflow stream occurs at the main septal meatus in between the turbinates in the anterior nose and moves forward through the middle of the nasopharyngeal meatus (Table 2). Examination of the velocity contours in the coronal sections, which lie in the intermediate range on the anterior-to-posterior axis, reveals a secondary peak of air speed ≅ 20 cm/s in the most dorsal area of the medial meatus. This is the S-shaped stream described above which flowed along the nasal roof to reach the ethmoid recesses, turned backward, and traveled ventrally before it finally exited through the dorsal part of the nasopharyngeal meatus. Velocities in the lateral and ethmoid meati were predicted to be much lower than in the main meatus (Figure 5). Flow patterns changed very little as $Q_{/2,\ insp}$ varied between 126 and 504 ml/min.

Flow distribution

The velocity profiles for predicted inspiratory flow were integrated over selected coronal sections to determine the

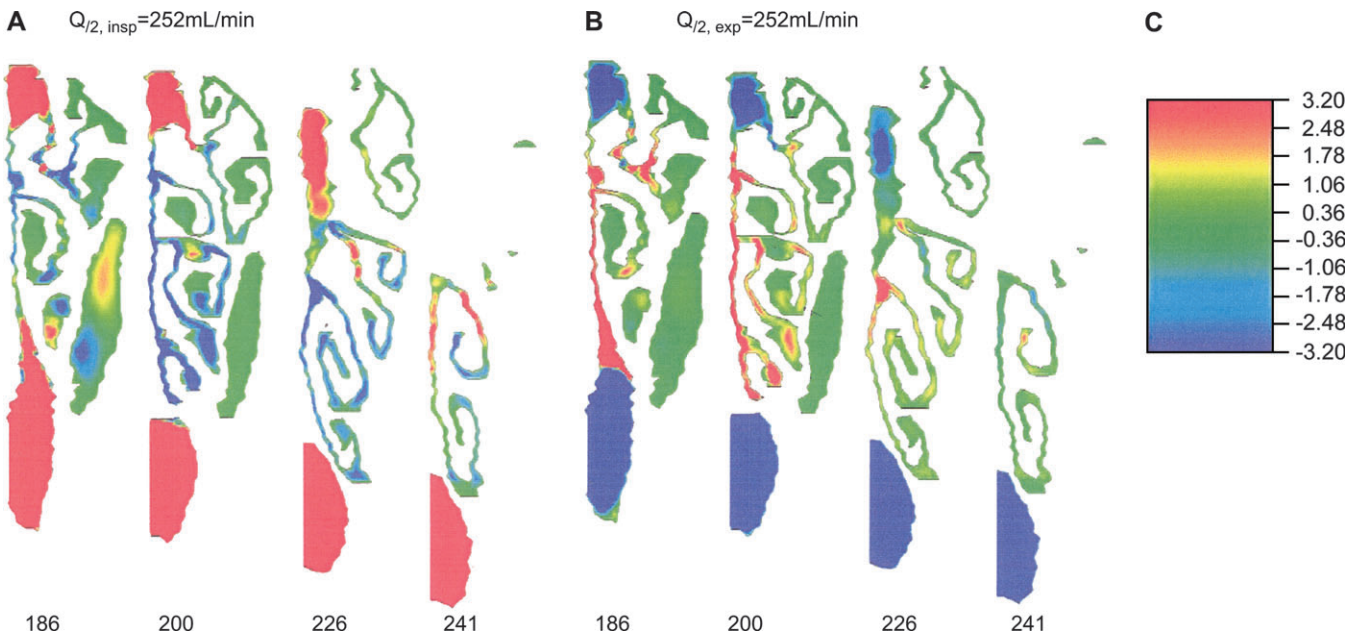

Figure 4 **(A)** Isovelocity contours for the axial velocity component (red indicates flow out of the paper) in the 4 coronal planes (186, 200, 226, and 241; from left to right—anterior to posterior) at $Q_{/2,\ insp}$ = 252 ml/min. Each individual coronal section is bounded by the bony septum to its left. **(B)** Isovelocity contours for the axial velocity component (blue indicates flow into the paper) at the same $Q_{/2}$ during expiration. Note that the color contour patterns are seen reversed as the positive velocity is defined as flowing out of the paper for both flow directions. **(C)** A restricted scale is used to better visualize the negative velocity in the ventral and lateral meati in the ethmoid recesses. Velocities higher than 3.2 cm/s or lower than –3.2 cm/s are represented by the most extreme colors in the color spectrum—red and dark blue—respectively.

Table 2 Percentage of volumetric flow distribution in our inspiratory simulation

Plane	Flow rate (ml/min)	Substreams						
		DM	DL	M	ML	VL	VM	NP
126 (K6)	126	29.9	16.1	26.1	NA	5.5	22.4	NA
	252	31.5	15.9	24.6	NA	5.7	22.3	NA
	504	32.1	14.8	23.1	NA	5.5	24.5	NA
200 (K23)	126	80.1	6.9	−1.2	0.9	−16.8	−69.9	100
	252	79.9	6.7	−1.3	0.8	−17.3	−68.2	99.4
	504	80.5	6.9	−1.3	0.8	−17.7	−67.4	98.2

NA, not applicable; ML, middle lateral; NP, nasopharyngeal meatus. Total airflow during 3 inspiratory flow rates is partitioned into various substreams (see Figure 6). Note percentages add to 100% for plane 126 and to approximately 0% for plane 200 where reverse flow occurs (see also caption of Table 3).

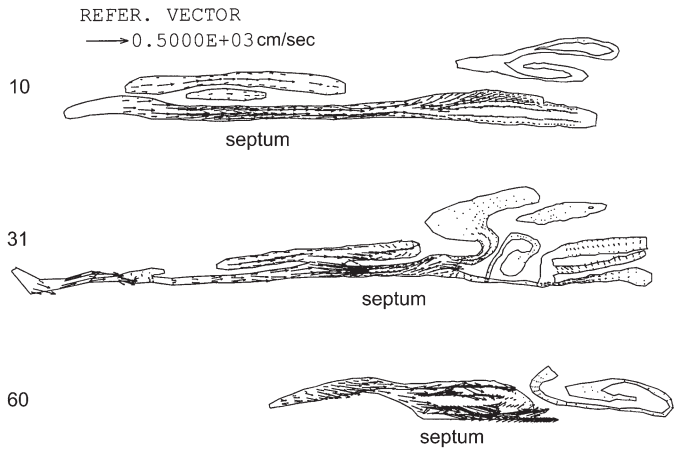

Figure 5 Inspiratory velocity vector plots on horizontal planes 10, 31, and 60 of the right nasal cavity at the half-nasal flow rate of 504 ml/min—looking up from below. Most air velocity is approximately in the plane of the paper and with direction and magnitude as shown by the vectors. Reference vector is given as 500 cm/s. External nares are to the left.

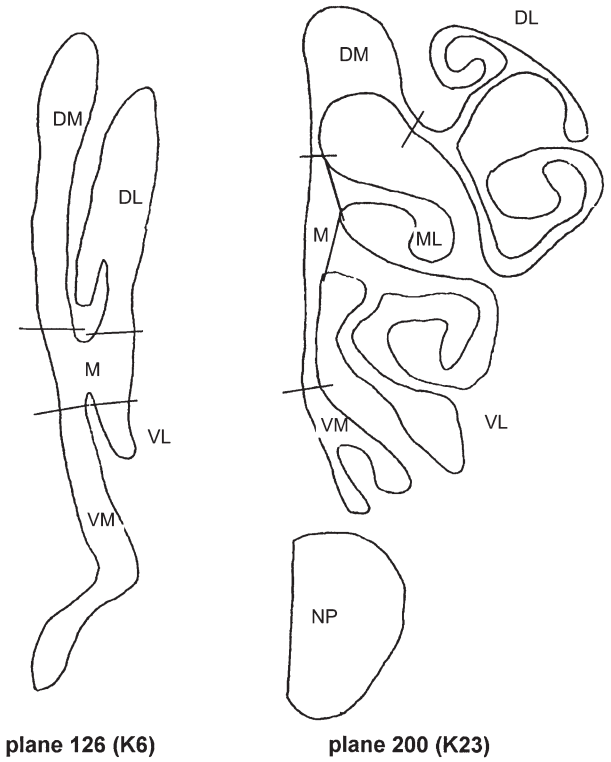

Figure 6 Coronal planes 126 (K6) and 200 (K23) divided into alphabetically labeled subsections. DL = dorsolateral, DM = dorsomedial, M = middle, VL = ventrolateral, VM = ventromedial, ML = middle lateral, and NP = nasopharyngeal meatus.

volumetric flow distribution throughout the nasal cavity. Flow rate over a given cross section is determined by integrating $\int(u_i \cdot n_i)\mathrm{d}A$ over each of the subsections, where u_i is the velocity component and n_i is the unit normal vector to each finite element face within the defined region. The volumetric flow rates through various subsections of coronal planes 126 and 200, corresponding to K6 and K23 (Figure 6), were calculated and normalized against total volumetric flow for the 3 flow rates simulated (Table 2) and compared reasonably well with the results of Kimbell and colleagues (Table 3). As the inspiratory flow rate increased, the percentage of reverse flow in the VM stream—the S-shaped streamlines—remained high. The implications of this lack of increased flow rate effect are discussed below.

Expiratory flow

Streamlines

In simulating the streamlines during expiration, neutrally buoyant particles were introduced at the posterior end of the nasopharyngeal meatus in a similar fashion as described for inspiratory flow. S-shaped streamlines entering the olfactory turbinate region were not evident (Figure 7).

Velocity profiles

Both plug flow and parabolic velocity profiles were applied at the nasopharyngeal meatus for simulated expiratory flow. No significant downstream difference in velocity field was found for the 2 different input velocity profiles. The distribution of the flow (Figure 4B) was qualitatively similar to that of the inspiratory flow at the same flow rate, but retrograde flow in the VM and VL regions was much less pronounced as total flow rate increases. The location of the peak velocity for the expiratory flow was similar, but the magnitude was smaller than for the inspiratory flow, which implies that expiratory flow was more uniformly distributed across the coronal section.

Velocity vectors in selected horizontal planes for 126 and 504 ml/min during expiratory flow were generally similar

Table 3 Percentage of volumetric flow distribution in Kimbell's inspiratory simulation

Plane	Flow rate (ml/min)	Substreams							
		DMS	DMN	DM	DL	M	ML	VL	VM
126 (K6)	100	12.9	2.6	NA	35.6	29.9	NA	0.9	11.5
	144	13.5	2.6	NA	37.7	26.8	NA	0.9	11.7
	200	13.8	2.7	NA	38	26.1	NA	0.9	11.7
	288	14.3	2.7	NA	38	25.5	NA	0.9	11.6
	400	15	2.8	NA	37.6	25.1	NA	0.9	11.6
	576	16.2	3	NA	36.2	24.8	NA	0.9	11.7
200 (K23)	200	NA	NA	91.9	7	−8.1	0.6	−17.4	−74
	288	NA	NA	91.8	7.2	−7.8	0.6	−17.4	−74.4
	400	NA	NA	92.1	7	−7.3	0.6	−17.9	−74.5
	576	NA	NA	92.3	6.9	−6.9	0.5	−18.7	−74.1

NA, not applicable; ML, middle lateral. Note that the substreams DMS (dorsal medial meatus adjacent to septum) and DMN (dorsal medial meatus adjacent to middorsal nasoturbinate) for level K6 are compared to our substream DM in plane 126. For plane 126, percentages add to 100% because all flows are moving in the same direction. For plane 200, percentages add to 0% due to equal percentages of forward and reverse flow in the absence of the nasopharynx.

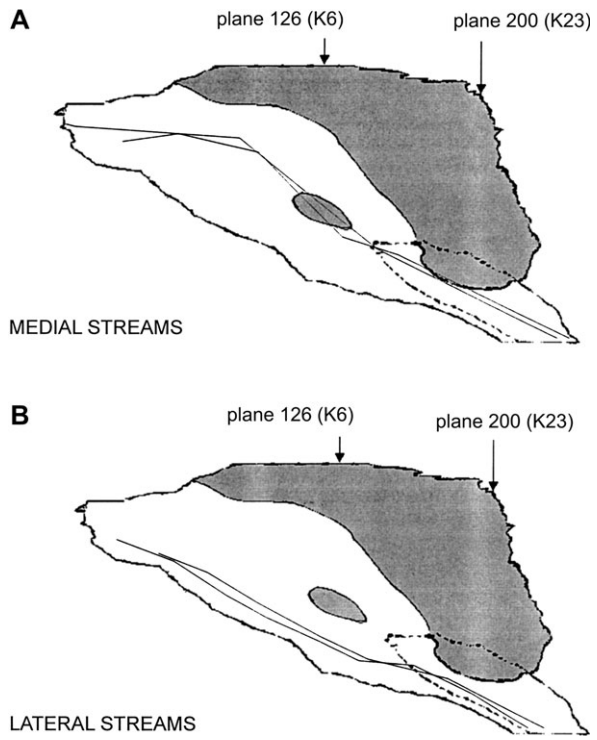

Figure 7 Simulated trajectories of the major expiratory flow streamlines at $Q_{/2,\ exp}$ = 504 ml/min. Streamlines were traced by releasing the particles near **(A)** the dorsal wall and **(B)** the ventral wall of the nasopharyngeal meatus. The streamlines are defined locally as the plane of nasopharyngeal meatus is the plane for particle release during expiration.

in magnitude, whereas opposite in direction to those for inspiratory flow. The magnitude of velocities in the lateral and ethmoid meati was predicted to be much lower than in the main meatus. Overall, the predicted flow patterns changed very little as $Q_{/2,\ exp}$ varied between 126 and 504 ml/min.

Flow distribution

The velocity profiles for the expiratory flow were also integrated in the same manner as for the inspiratory flow to determine the volumetric flow distribution. The regional stream flow rates were normalized against total volumetric flow for the 3 expiratory flow rates (Table 4). Six major streams during expiratory flow—DM, DL, M, middle lateral (ML), VM, and VL—were predicted in the anterior and posterior nose, similar to inspiratory flow. For low total nasal flow rate, a large fraction of negative retrograde (back toward the nasopharyngeal meatus) was simulated on expiration in the VM and middle (M) streams (Figure 4B). This retrograde flow fraction decreased as total nasal flow increased (Table 4).

Discussion

Our finite element mesh was reconstructed from horizontal cast sections rather than from coronal sections as used by Kimbell et al. The flow distribution for plane 200 from our model was generally in good agreement with the results of Kimbell et al. In plane 126, the flow distribution showed the dorsal flow differed (~45%) from what was reported by Kimbell (~52%). Because the flow rates used in both models were not the same and the flow distribution calculation was not exactly the same, the results may not be directly comparable.

Table 4 Percentage of volumetric flow distribution in our expiratory simulation

Plane	Flow rate (ml/min)	Substreams						
		DM	DL	M	ML	VL	VM	NP
126 (K6)	126	−29.3	−14.4	−26.1	NA	−5.5	−24.7	NA
	252	−29.1	−14.2	−25.1	NA	−5.8	−25.8	NA
	504	−28	−13.1	−25.9	NA	−5.5	−27.5	NA
200 (K23)	126	−81	−6.9	−1.3	0.2	17.8	71.5	−100
	252	−72.3	−6.7	−1.5	0.3	17	63.2	−100
	504	−34.5	−6.8	0.3	−0.2	9.2	32.1	−100

NA, not applicable; ML, middle lateral; NP, nasopharyngeal meatus. Total airflow during 3 expiratory flow rates is partitioned into various substreams (see Figure 6). Percentages add to −100% for plane 126 and to approximately 0% for plane 200 where reverse flow occurs similar to data in Tables 2 and 3.

To test for convergence of the numerical solution for the velocity field, we doubled the total number of nodes for both inspiratory and expiratory flow and saw no significant change in velocity profiles. The current total node number of ~130 000 should therefore be sufficient to simulate the airflow under the physiological flow conditions being investigated.

As mentioned in the Materials and Method section, the mesh of the airspace near some ethmoid turbinates did not appear complete after reconstruction. The impact on the overall velocity distribution in the nasal cavity is likely to be small as the velocity in the olfactory region is low, and the resultant change would be negligible.

Simulated reverse flow became less prevalent as the flow rate increased in expiratory flow but remained quite large for all 3 inspiratory flow rates. This is due to the geometry of the nasopharyngeal meatus, which most likely results in inertial forces preventing the streamlines from bending to curve up into the olfactory region on expiration. Fully unsteady flow calculations will be necessary however to completely investigate this effect. The airflow is complicated due to the complex geometry of the ethmoid turbinates; however, from looking at both the sagittal and coronal velocity magnitudes, one can see where the flow is reversed (or negative) and where it is moving toward the pharyngeal tube (or positive). The implications of the effect for the nasal cavity geometry on the reverse flow for species during evolution remain to be explored.

The predicted fraction of volumetric flow reaching the olfactory region changed with flow rate for both inspiratory and expiratory flows. As the flow rate increased, the percentage of simulated flow in the DM stream increased slightly for inspiration and decreased greatly for expiration.

This difference, along with the flow distribution difference noted above, is consistent with sniffing effectiveness in rodents as proposed by Youngentob et al. (1987) in that odorant molecules inhaled during the inspiratory sniff phase can be trapped and not washed out on the expiratory phase, thereby increasing the time available for odorant molecules to interact with the ORs. Indeed, our results suggest that as the rat increases the flow rate from normal breathing to medium sniffing and even maximal sniffing, an increased number of molecules may reach the olfactory region and increase the effectiveness of odorant discrimination. To adequately answer this question, fully unsteady calculations are required. However, given the step-like geometry of the olfactory region, it is likely that odorant wash-in during inspiration will not be completely washed out during expiration. Low-speed expiratory flow (as is present at the beginning of expiration) may indeed wash out some of the olfactory recesses. This remains to be investigated by doing fully unsteady (time dependent) flow simulations in the rat nose of the whole cycle of inspiration and expiration. At present, this cannot be achieved due to speed limitations in our computer, but we are looking forward to investigating this question soon.

Appendix: Numerical Simulation of Airflow

The Reynolds number N_{Re} in the rat nasal cavity is defined as Ud/ν, where U is the average air velocity just inside the rat external naris, d (0.18 cm) is the hydraulic diameter (= 4× area/perimeter) of the external naris, and ν is the kinematic viscosity of air (0.157 cm^2/s). Because air density, viscosity, and diffusivity are assumed to be constants and the geometry of the model is fixed, N_{Re} depends only on the average air velocity U, which is equal to the quotient of $Q_{/2}$, the half-nasal flow rate, divided by A, the cross-sectional area of the external naris.

The dimensionless Strouhal number N_{St} in the rat nasal cavity is defined as $\omega L/U$ (Grotberg 1990). The parameter L is a characteristic length (the longitudinal path length or the axial length) along the nasal cavity, and ω (= $2\pi f$) is the angular breathing (or sniffing) frequency. During maximal sniffing, N_{St} is estimated to be 0.39 based on the values of $f \cong 8$ Hz, $L \cong 3$ cm, and $U \cong 380$ cm/s (Youngentob et al. 1987). For normal breathing at rest, $f = 1.15$–1.7 Hz, $U \cong 70$ cm/s (Mauderley et al. 1979), and N_{St} is estimated to be 0.31–0.46. The average air velocity at the external naris in the rat nose is based on a cross-sectional area there of 0.025 cm^2. Values of the Strouhal number less than 1.0 indicate that the flow behaves as if it were approximately steady with time-dependent acceleration forces small compared with viscous and inertial forces.

Acknowledgements

The authors would like to thank Gordon Neufeld and his staff at the Philadelphia VA Medical Center for their efforts in providing and sectioning the rat nasal cavity cast and the photomicrographs of the sections. We also acknowledge valuable comments of the reviewers on the manuscript. This work was supported by the National Institute of Deafness and Other Communication Disorders grant NIDCD-00072.

References

Grotberg JB, Sheth BV, Mockros LF. 1990. An analysis of pollutant transport and absorption in the pulmonary airways. J Biomech Eng. 112:168–176.

Kelemen G. 1947. The junction of the nasal cavity and the pharyngeal tube in the rat. Arch Otolaryngol. 45:159–168.

Kimbell JS, Fleishman A, Andersen ME, Morgan KT. 1990. Determination of nasal airflow characteristics in F-344 rats and rhesus monkeys and application to inhalation toxicology. Toxicologist. 10:259.

Kimbell JS, Godo MN, Gross EA, Joyner DR, Richardson RB, Morgan KT. 1997. Computer simulation of inspiratory airflow in all regions of the F344 rat nasal passages. Toxicol Appl Pharmacol. 145:388–398.

Kimbell JS, Gross EA, Joyner DR, Godo MN, Morgan KT. 1993. Application of computational fluid dynamics to regional dosimetry of inhaled chemicals in the upper respiratory tract of the rat. Toxicol Appl Pharmacol. 121:253–263.

Mauderly JL, Tesarek JE, Sifford LJ, Sifford LJ. 1979. Respiratory measurements of unsedated small laboratory mammals using nonrebreathing valves. Lab Anim Sci. 29:323–329.

Mery S, Gross EA, Joyner DR, Godo M, Morgan KT. 1994. Nasal diagrams: a tool for recording the distribution of nasal lesions in rats and mice. Toxicol Pathol. 22:353–372.

Morgan KT, Kimbell JS, Monticello TM, Patra AL, Fleishman A. 1991. Studies of inspiratory airflow patterns in the nasal passages of the F344 rat and rhesus monkey using nasal molds: relevance to formaldehyde toxicity. Toxicol Appl Pharmacol. 110:223–240.

Patra AL, Gooya A, Morgan KT. 1986. Air characteristics in a baboon nasal passage cast. J Appl Physiol. 61:1959–1966.

Pedley TJ, Schroter RC, Sudlow MF. 1977. Gas flow and mixing in airways. In: West JB, editor. Bioengineering aspects of the lung. New York: Marcel Dekker, Inc., p. 163–265.

Ring G, Mezza RC, Schwob JE. 1997. Immunohistochemical identification of discrete subsets of rat olfactory neurons and the glomeruli that they innervate. J Comp Neurol. 388:415–434.

Schreider JP. 1983. Nasal airway anatomy and inhalation deposition in experimental animals and people: In: Reznik G, Stinson SF, editors. Nasal tumors in animals and man. Vol. 3. Experimental nasal carcinogenesis. Boca Raton (FL): CRC Press. p. 1–26.

Uraih LC, Maronpot RR. 1990. Normal histology of the nasal cavity and application of special techniques. Environ Health Perspect. 85:187–208.

Whitaker S. 1992. Introduction to fluid mechanics. Malabar (FL): Krieger Publishing Co. 474 p.

Yang CC. 1999. Numerical modeling of odorant uptake in the rat and bullfrog nasal cavities (Ph.D. dissertation). Philadelphia (PA): University of Pennsylvania.

Youngentob SL, Mozell MM, Sheehe PR, Hornung DE. 1987. A quantitative analysis of sniffing strategies in rats performing odor detection tasks. Physiol Behav. 41:59–69.

Zhao K, Dalton P, Yang GC, Scherer PW. 2006. Numerical modeling of turbulent and laminar airflow and odorant transport during sniffing in the human and rat nose. Chem Senses. 31:107–118.

Accepted November 16, 2006